Nanoseismic measurement of the localized initiation of sliding friction

Gregory McLaskey & Steven Glaser
Department of Civil and Environmental Engineering, University of California, Berkeley, USA

ABSTRACT: This paper presents theoretical and experiments results of nanosesimic waves generated from frictional sliding and recorded by an array of high-fidelity Glaser-NIST nanoseismic sensors. Absolute sensor calibration procedures are reported along with some preliminary experimental findings. Estimating seismic source characteristics given an array of recorded signals and the specimen's Green's function is an inverse problem formulation that has been successfully used for the study of earthquake source mechanisms, and to distinguish between earthquakes and underground explosions. When properly scaled, the study of nanoseismic sources can shed light on frictional behaviors at both very small and earthquake fault scales. The preliminary experiments, from a PMMA slider on a large PMMA plate, demonstrate that local force release on the friction surface can be detected on a number of different time and amplitude scales. For rapid load releases (on the order of 500 ns) the source location can be estimated to a few mm in space and μs in time for step-like source functions down to about 10 mN in amplitude. Load releases which occur less rapidly in time (on the order of 100 μs) or over a larger spatial area (larger than a few mm) are more difficult to identify and interpret. Absolute calibration on a PMMA plate shows that the sensors have a sensitivity of 15 mV/nm ± 4 dB over a frequency range of approximately 20 kHz to 1 MHz. The calibrated noise floor for the sensors is ± 15 pm.

1 INTRODUCTION

From the wear of our teeth, to earthquake hazards, to new nano-machines which require an understanding of friction at the atomic scale, the effects of friction are far reaching. At all scales, most of the mechanical energy sapped by friction is converted into thermal phonons at THz frequencies (e.g. Sevinçli 2008, Krim et al. 1991), but some small portion is converted to seismic waves which travel through the material and are manifested as the screech of brakes, the squeal of sliding rubber, earthquake ground motions, and nanoseismic vibrations. We have devised a laboratory-based nanoseismic measurement and interpretation technique which allows us to measure elastic waves radiated from load releases due to slippage on the micro- and possibly nano-scale, and the results may be scaled up to shed light on earthquake-scale sliding.

A number of different models of friction, describing a large range of length scales are illustrated in Figure 1. On one hand, a mechanistic study of friction will by necessity reduce to understanding inter-atomic forces and motions on the order of nm. On the other hand, the behavior of earthquake faults is measured over length scales of km, and at this scale (the macro-scale) all the way down to a human scale (the meso-scale), frictional force is defined by the so-called Coulomb (1779) friction model, the behavior of which has been directly observed since Da Vinci. As the micro-scale is approached, the friction model of Bowden & Tabor (1954) is more suitable. Their applications were lubricated shafts and cutters, gears and connecting arms. They posited quasi-static junctions, with an average area of contact, and a wear-free interface. The Bowden-Tabor model, however, cannot account for micro-mechanical behaviors and does not predict thousands of recent micro-and nano-scale measurements. For example, behaviors such as cold welding, plastic deformation (Muser 2001), and adsorbed sub-monolayers of so-called third species from the environment, e.g., oxidation, can control junction shear resistance (e.g. Krim, 1991). The junction behaviors scaling up from the nano (atomic bonds) and scaling down from the micro should at some point agree, yet few researchers even address this issue.

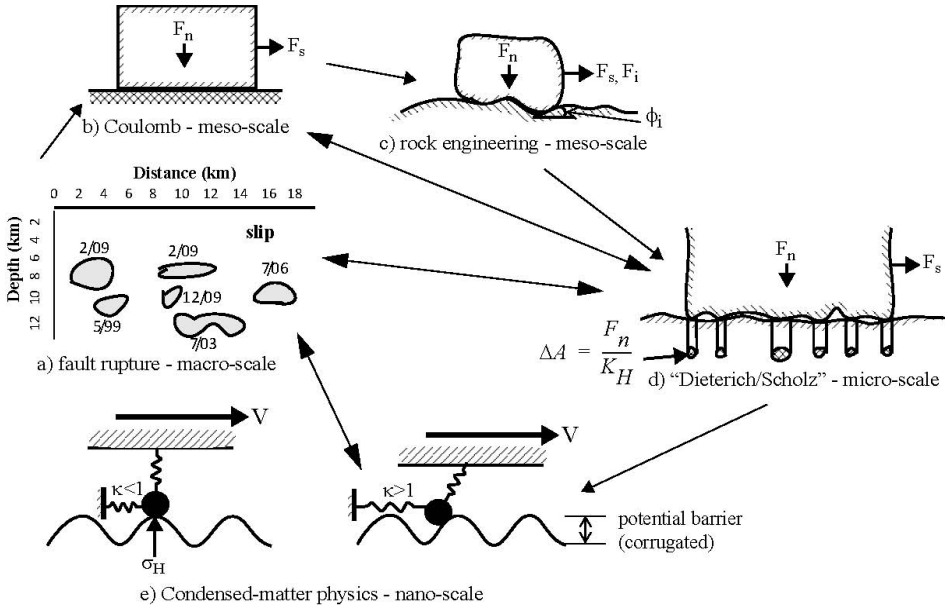

Figure 1. Models of multi-scale sliding friction. Macro- and meso scale models are behavioral criteria that accurately predict behavior on that scale. The micro-scale model posits a physical mechanism.

Apart from obvious differences in length scale, there is a phenomenologically self-similar behavior amongst many different scales. For example, a common atomistic model is the Frenkel-Kontorova-Tomlinson model (Weiss & Elmer 1997), Fig 2a, where atoms in a body are considered as point bodies with spring-like inter-atomic bonds connecting to other atoms in all six Cartesian directions. On the other hand, a common seismological model is the Burridge-Knopoff (1967) model, Fig. 2b, where coherent bodily lengths are modeled as sliding blocks connected to other blocks by springs in all six Cartesian directions. The pinning of junctions on different scales have different apparent physical mechanisms but serve the same purpose—minimum energy attractors (Weiss & Elmer 1997). The physical scale at which the stick-slip transition appears to takes place gets smaller and smaller as instrumentation improves.

While a small specimen may appear to respond to sliding as a single block, slip on an earthquake fault cannot happen simultaneously along a km-scale length—stress information cannot move through the earth faster than the speed of sound. The fault must be broken down into multiple sections such as in the Burridge-Knopoff model. Very large sliding bodies such as faults are too large to be treated as a point mass. This limit is defined by the elastic coherence length, ξ. During slow-velocity sliding, only volume elements of dimensions about ξ will displace coherently (Persson 1998). The coherent length ξ becomes smaller as normal stress on the joint becomes larger or the materials become more compliant, and the multiple volume elements making up a sliding block can have individual stick-slip motions. This theory can explain much of earthquake fault mechanics, in particular questions brought up about self-healing slip and the foam rubber models (e.g. Hartzell & Archuleta 1979, Perrin et al. 1995, Heaton, 1990).

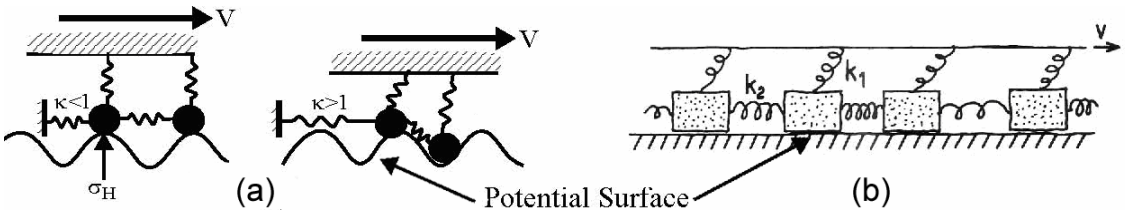

Figure 2. Condensed-matter physics and earthquake fault models of frictional interaction. A single contact junction is shown on the left, and multiple junction model is shown on the right -the Burridge-Knopoff model of 1967 (from Persson 1998).

The local stress change at a breaking junction travels through the material as a stress wave. If all the atomic contacts making up a junction are slipping fast enough and with sufficient coherency, high frequency (well into the MHz range) stress waves will radiate away from the junction and through the material at the speed of sound. These nanoseismic events carry the time stress history of the junction rupture dynamics. Very careful recording and analysis of these signals can provide a glimpse of the in situ junction dynamics for a meaningful situation, providing an acoustic microscope of exquisite sensitivity—picometer displacements over a frequency bandwidth of 20 kHz to over 1 MHz. This paper reports on the initial sliding friction tests using our high-fidelity sensors and inversion techniques.

With the techniques outlined in this paper, we can measure changes in the local force field at the location of an individual breaking junction. Careful application of this toolset can provide new insights into dynamic behaviors at the micro-scale and sub-micro "disconnect" scale which exists between micro- and nano-scales. These insights, in turn, may also pertain to the macro-scale since the effective length scale of experiments performed in the lab can be adjusted by scaling material properties, and normal loads. Brune (1973) modeled km of faults with cm of foam rubber.

2 BACKGROUND AND PROBLEM FORMULATION

The study of waves propagating through solids has its beginnings in the theoretical work dating back to the 19th century (e.g. Rayleigh 1887, Lamb 1904 , Love 1934), and more recent experimental work has confirmed theoretical findings (e.g. Aki & Richards 1980, White 1965). The elastodynamics of stresses and strains which govern elastic wave propagation in a solid body can be described by Navier's equation, which can be derived (Graff 1975) by substituting the appropriate definition for strain and the stress-strain relationship into the stress equations of motion:

$$\rho \frac{\partial^2 u_i}{\partial t^2} = f_i + (C_{ijkl}(u_{k,l} + u_{l,k})/2)_{,j} \tag{1}$$

where u_i is the displacement vector of a material point, ρ is the density of the material, C_{ijkl} is the fourth order elastic strain tensor, and f_i is a body force applied to the material. For this work, we seek solutions in the form of a Greens function $G_{in}(x,t,\xi,\tau)$, which is the displacement at point x at time t due to a unit impulse at location ξ in the direction n at time τ (Aki & Richards 1980) . The Green's function is a symmetric second order tensor which must satisfy Equation 1, specifically:

$$\rho \frac{\partial^2 G_{in}}{\partial t^2} = \delta_{in}\delta(\mathbf{x}-\xi)\delta(t-\tau) + (C_{ijkl}G_{kn,l})_{,j}\,. \tag{2}$$

The Green's function can be thought of as the impulse response function of an elastic material that maps the dynamic force field at location ξ to a mechanical disturbance u_i at the sensor site x. Once the Green's function is known, the material response to an arbitrary force time function can be calculated via convolution.

Under the definition of the Green's function, the displacement at the transducer location can be expressed as

$$u_i(\mathbf{x},t) = \int_{-\infty}^{\infty} \iiint_V G_{in}(\mathbf{x},t;\boldsymbol{\xi},\tau) f_n(\boldsymbol{\xi},\tau)\, dV\, dt \tag{3}$$

where V is the source volume which contains non-zero portions of f_n. If the source volume is replaced by a point ξ^0, the Green's function can be expanded in a Taylor series about this point (Stump & Johnson 1977). By taking only the first two terms of this series, we can write

$$u_i(\mathbf{x},t) = G_{in}(\mathbf{x},t;\xi^0,\tau) * F_n(\xi^0,\tau) + G_{in,j}(\mathbf{x},t;\xi^0,\tau) * M_{nj}(\xi^0,\tau) \tag{4}$$

where $*$ represents convolution in time, the force vector

$$F_n(\xi^0,\tau) = \int_V f_n(\xi,\tau)dV\,, \tag{5}$$

and the force moment tensor

$$M_{nj}(\xi^0,\tau) = \int_V x_j f_n(\xi,\tau)dV\,. \tag{6}$$

Our objective is to represent the source using the vector-valued function $F_n(\tau)$ and the tensor valued function $M_{nj}(\tau)$ at the location $\xi^0$of a locked asperity, and to relate this to source characteristics and the mechanisms and dynamics of friction.

Following a transfer function calibration approach (fully described in Hsu & Breckenridge 1981), the transducer output v(t) can be expressed as the linear convolution of the surface displacement and the transducer's instrument response function:

$$v(t) = u_i(\mathbf{x},t) * i(t)\,. \tag{7}$$

By inserting Equation 4 into Equation 7 and applying a Fourier transform to the result, we find

$$V(\omega) = I(\omega)[F_3(\xi^0,\varpi)G_{in}(\mathbf{x},\omega;\xi^0,\varpi) + G_{in,j}(\mathbf{x},\omega;\xi^0,\varpi)M_{nj}(\xi^0,\varpi)]\,. \tag{8}$$

and the complex transfer function of the transducer can be found by inversion:

$$I(\omega) = V(\omega)u_i^{x_0}(\omega)^{-1}\,. \tag{9}$$

Equation 9 can be reformulated into the form

$$\mathbf{V}(\omega) = \mathbf{I}(\omega)\mathbf{M}(\xi^0,\varpi)\mathbf{G}(\mathbf{x},\omega;\xi^0,\varpi)\,. \tag{10}$$

Where $\mathbf{V}(\omega)$ is a vector which includes the real and imaginary components of the voltage output at a particular frequency ω and has dimensions 2n for the case of an array of n sensors, $\mathbf{I}(\omega)$ is a 2n by 2n diagonal matrix whose elements are the real and imaginary components of the instrument response function for sensor n at frequency ω, $\mathbf{M}(\xi^0,\omega)$ is a vector of length 2m which contains the real and imaginary components of the force vector and moment tensor elements which are to be determined, and $\mathbf{G}(x,\omega,\xi^0,\varpi)$ is a 2n by 2m matrix composed of the real and imaginary components of the appropriate Green's function for sensor n and force/moment element m at frequency ω (see also Stump & Johnson 1977).

Under this formulation, the m elements of the force vector and moment tensor at each Fourier frequency can be found by inversion given the voltage outputs from an array of n sensors, the instrument response function for each sensor, and the appropriate Green's function for each combination of the force/moment elements and sensor locations.

A number of strategies may be employed to solve for the Green's functions either analytically (typically with the use of Fourier and Laplace transforms) or numerically. Closed form solutions currently exist for the whole space (e.g. White 1965, Aki & Richards 1980), half space (Pekeris 1955), and infinite plate (Johnson 1974). For this work, a solution scheme known as generalized ray theory has been used for an infinite plate geometry (Helmberger 1974, Ceranoglu & Pao 1981). This solution was checked against the theoretical solutions of Knopoff (1958) and Pekeris (1955).

3 SENSOR ARRAY

A number of different types of sensors have been employed for the detection of small-amplitude high-frequency surface displacements, such as those expected to result from frictional sources. These sensors include those developed for ultrasonic, microseismic, and acoustic emission applications. Following the solution strategy described in the previous section, absolute measurement of surface displacements at an array of sensor locations is required, and it is also desirable to use a sensor which has excellent sensitivity, a wide bandwidth, and near-flat frequency response. While much of the quantitative experimental work to date has made use of capacitive (e.g. Breckenridge et. al 1975, Kim & Sachse 1986, Hsu & Hardy 1978) or optical (Eisenhardt

et al. 1999, Scruby & Drain 1990) transducers, the sensitivity requirements warrant the use of piezoelectric devices. Most piezoelectric sensors take advantage of some mechanical resonance to gain high sensitivity at the expense of loss of bandwidth and signal distortion, but a piezoelectric sensor with a large backing mass and conical piezoelectric element was designed in the late 1970s to provide a more faithful transduction of surface displacement (Proctor 1982, Greenspan 1987). This sensor is reported to have an extremely flat amplitude response between 100 kHz and 1MHz. The Glaser-NIST transducers employed for this study are based on this original concept but were further developed in our laboratory. (For more details see Glaser et. al 1998, To & Glaser 2005, McLaskey et al. 2007.)

3.1 *Sensor Calibration*

The sensor transfer function calibration approach used for this work follows the traditional experimental design carried out by acoustic emission researchers at the NBS in the late 1970s (Breckenridge et. al 1975). In a typical calibration of this type, a number of assumptions are made whereby it is assumed that the transducer response function $i(t)$ can be modeled as a linear time-invariant system which maps a mechanical disturbance $u_i(\mathbf{x},t)$ to a transducer output $v(t)$ (Hsu & Breckenridge 1981). This system's transfer function can be estimated in the frequency domain from Equation 9 by directly dividing the complex-valued spectral estimates of the sensor output by those of the input (surface displacements at the location of the sensor).

To characterize the sensor in this manner, the exact mechanical disturbance (i.e. the displacement $u_i(\mathbf{x},t)$ of the surface of the specimen which would exist in the absence of the sensor) must be known. This is found theoretically by using a "known" source and a test block for which the Green's function is known. The test block used in these calibration experiments was a massive, polymethylmethacrylate (PMMA) plate 50 mm thick and 940 mm square. The sensor location was chosen to be in the center of the plate directly beneath the source location, on the opposite side of the plate. Traveling at the compressional wave velocity in this material (measured to be 2.8 km/s), it takes approximately 330 μs for side reflections to return to the center of the plate where the source and sensor are located. In this time period, the plate can be treated as infinite and the Green's functions found from the infinite plate geometry can be applied to solve Equations 4 and 10.

The two "known" nanoseismic sources used for calibration purposes in this study are the fracture of a glass capillary tube and a ball impact. The capillary fracture is known to present a force time function into the test block which is very nearly equal to a step function with a rise time of less than 200 ns (Breckenridge et. al 1975). This source has been used by many researchers because the force at which the fracture occurs (and therefore the amplitude of the step) can be independently measured. The less-frequently used ball impact is known to introduce an impulse-like pulse into the material, and the change in momentum that the ball imparts to the transfer block can be independently measured. Starting with the work of Hertz (1882), a great deal of theoretical and experimental work concerning the collision of a sphere on a massive body has shown that the amplitude and frequency content of this pulse are functions of the ball size and impact velocity (Goldsmith 2001, Johnson 1985). Both of these sources are assumed to apply forces only in the direction normal to the surface of the test block.

The sensor output (experiment) and surface normal displacements (theory) due to a 0.4 mm diameter ruby ball dropped 0.325 m onto a 50 mm thick PMMA plate are shown in Figure 3 (a). The sensor is located directly beneath the location of impact, on the opposite side of the plate. The theoretical displacements are found from the convolution of the Green's function (G_{33}, where direction 3 is the direction normal to the plate) and appropriate pulse found from Hertz theory (400 mN tall and 2.8 us wide). The amplitude of the Fourier transform of these two time series is shown in Figure 3 (b) compared to the amplitude of the Fourier transform of a pure noise signal.

The same comparison (sensor output and normal displacements) are shown in Figure 4 for the case of a 0.250 mm diameter glass capillary tube loaded on its side and fracturing under a load of 9N. The sensor is again located directly beneath the location of impact, and the displacements are found from the convolution of the same Green's function as in Figure 3 with a step function of amplitude 9 N and rise time of 100 ns.

Following Equation 9, the instrument response function (or rather the complex transfer function of the sensor) can be found by dividing the Fourier transform of the sensor output (experiment) by the Fourier Transform of the normal displacements (theory). The amplitude (a) and phase (b) of the complex transfer function coefficients are plotted in Figure 5. This calibration shows that the sensor response is flat in amplitude to +/- 4 dB between 20 and 1000 kHz and nearly zero phase in the same frequency range. This transducer has sensitivity of about 15 mV/nm and the noise level is about +/- 15 pm. Both the ball drop and capillary fractures yield the same transfer function to within a few dB. This match validates both the step function capillary fracture model and the Hertzian impact model and illustrates the robustness of this calibration approach.

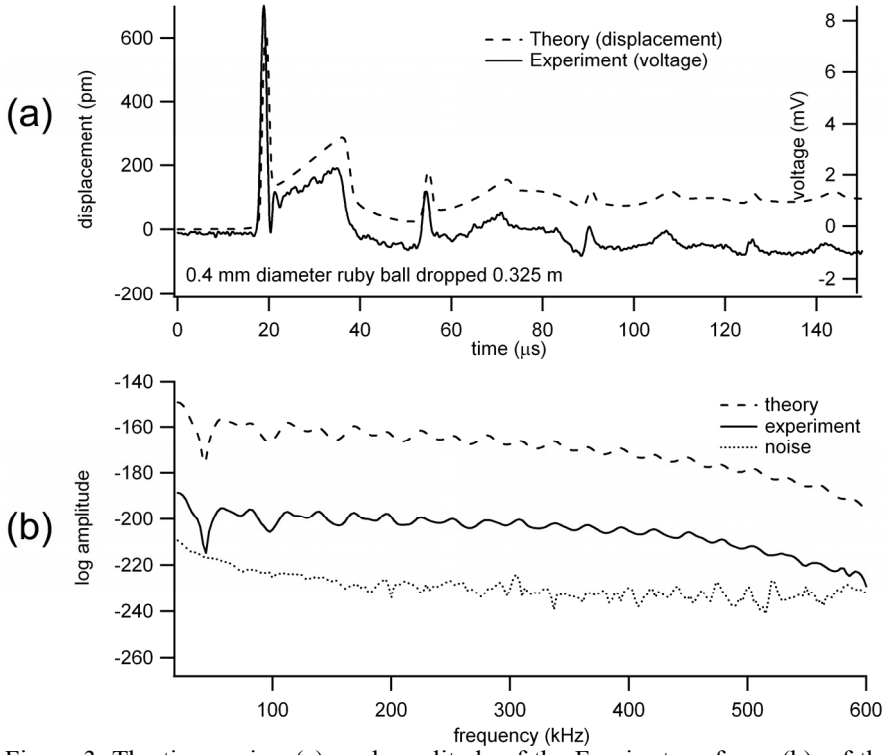

Figure 3. The time series, (a), and amplitude of the Fourier transform, (b), of the sensor output (experiment) and surface normal displacements (theory) due to a 0.4 mm diameter ruby ball dropped 0.325 m onto a 50 mm thick PMMA plate.

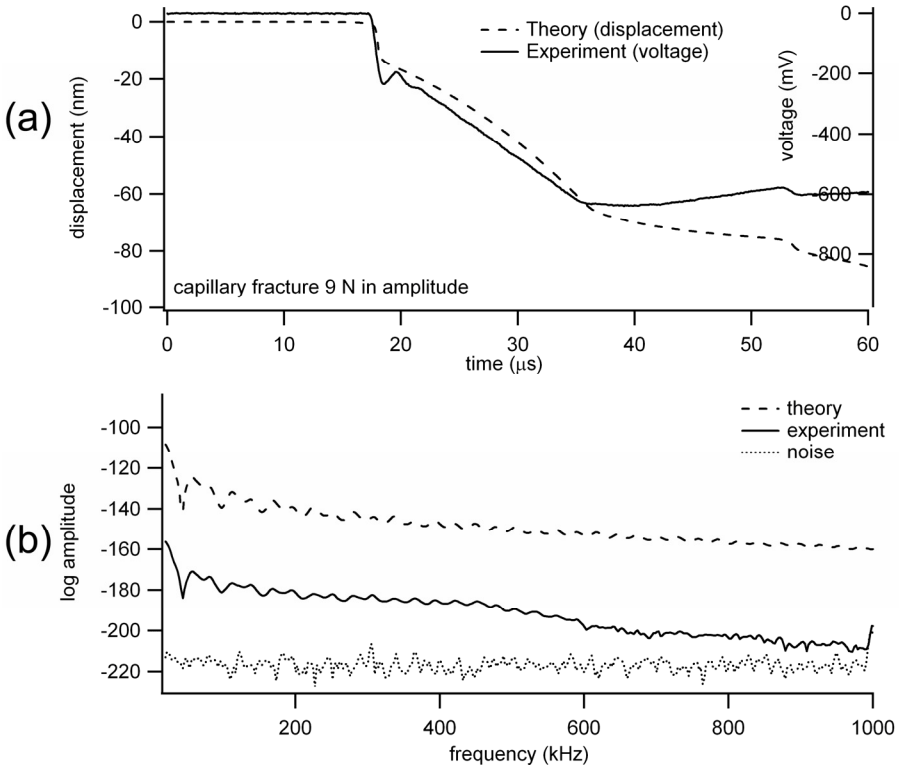

Figure 4. The time series, (a), and amplitude of the Fourier transform, (b), of the sensor output (experiment) and surface normal displacements (theory) due to the fracture of a 0.25 mm diameter glass capillary tube on a 50 mm thick PMMA plate. The capillary tube was loaded on its side and fractured at a load of 9N.

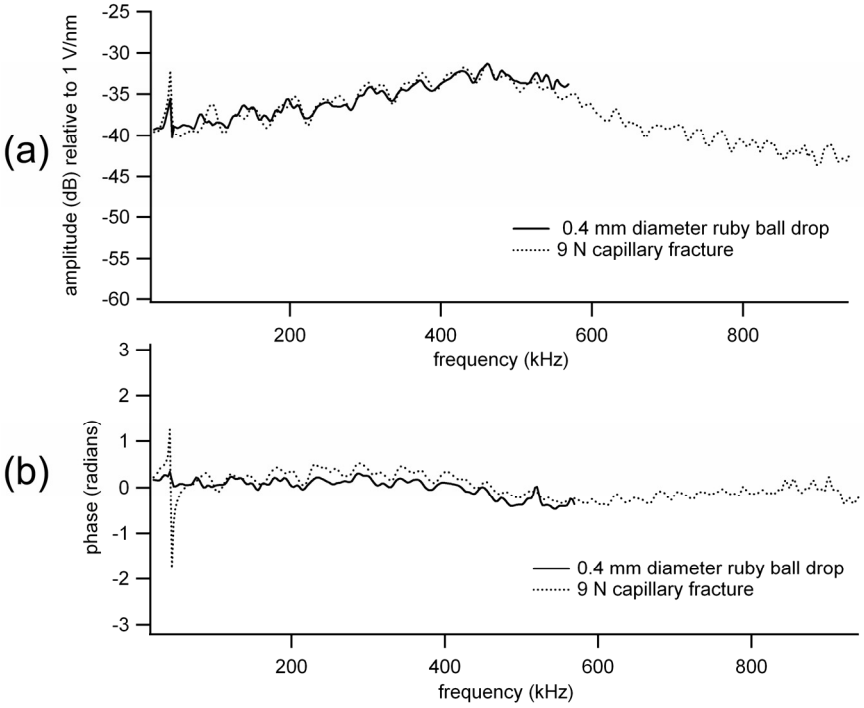

Figure 5. The amplitude, (a), and phase, (b), of the complex transfer function coefficients estimated from both the ball impact and capillary fracture sources.

4 EXPERIMENTAL SETUP

A set of experiments were performed in order to validate the effectiveness of the solution strategy outlined in Section 2. While the results are entirely preliminary in nature, their existence demonstrates the feasibility of the method, and they highlight some of the strengths and limitations of the approach.

The experimental setup, depicted in Figure 6, includes the 50 mm thick PMMA base plate (a), a slider block (b) (dimensions 120 mm by 12 mm by 50 mm in the 1, 2, and 3 directions, respectively), an array of Glaser-NIST sensors (c) located on the bottom side of the base plate, and sensor (d) which measures the displacement of the back end of the slider block relative to the base plate. The slider block is loaded vertically with a normal force on the order of 35 N and then loaded horizontally at the back end of the block as shown by the arrow in Figure 6. When slip occurs between the slider and base, the local shear forces overcome the locked asperities on the friction surface. This force release, depicted at the location (e) of the previously locked asperity, causes elastic waves (f) to propagate through the base plate and slider block until they are detected by the array of sensors.

With a plate thickness of 50 mm, a 1 N step force will produce a P-wave amplitude of about 1.5 nm at the location of sensor 1, therefore with a 15 pm noise level the smallest detectable step force will be about 10 mN. The location e of the source of the detected waves can be found from triangulation based on the differences of arrival times of various wave phases arriving at the known locations of each sensor in the array (Salamon & Wiebols 1974, Baron & Ying, 1987, Stein & Wysession 2003). Once the source location is found, Green's functions can be calculated for each sensor-source pair, and the components of the force vector $F_n(\tau)$ and moment tensor $M_{nj}(\tau)$ can be solved using Equation 10.

PMMA was chosen for both the slider and base materials because of its attenuative properties. Elastic waves above about 50 kHz propagating through this material will be highly attenuated after they have propagated more than a few hundreds of mm. This attenuation is great enough that all high frequency wave arrivals (greater than 50 kHz) felt by the sensors can be assumed to be direct arrivals from the frictional interface or nearby region. This keeps the wavefield free from high frequency reflections from the outside edges of the plate and allows the easy identification of high-frequency, short-wavelength elastic wave arrivals.

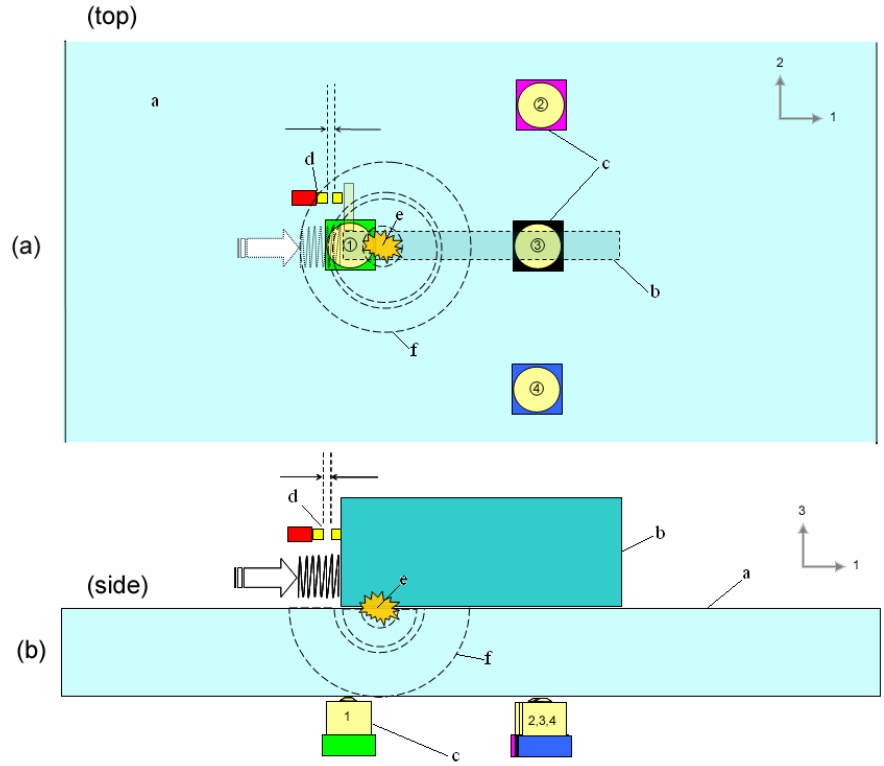

Figure 6. Schematic of the experimental setup: a, base plate; b, slider block; c, Glaser-NIST sensors; d, displacement sensor; e, example friction source location; f, radiated transient elastic waves.

5 PRELIMINARY RESULTS

The results shown in Figure 7 were obtained following the experimental procedure described in the previous section. These sensor outputs were obtained at the onset of frictional sliding and are offset for clarity. The curve labeled 'displacement' and shown in grey is a plot of the output of the displacement sensor (object (d) from Fig. 6). The other four traces are from an array of Glaser-NIST sensors whose general locations are depicted in Figure 6. Two distinct wave arrivals can be seen from this plot, one at a approximately 2.5 ms and the other at about 4.88 ms. These two wave arrivals, plotted in Figures 6 and 7 at different time scales, are illustrative examples of two different and reoccurring types of phenomena observed during these preliminary tests. The first arrival to occur, depicted in Figure 8, is felt by all four sensors, but appears to be a low frequency arrival with a rise time on the order of 100 μs. For this event, the P- and S-wave arrivals (which should be separated by about 20-30 μs for the source-sensor distances of this test setup) are smeared together by a long temporal duration of the source function $F_n(\tau)$ and/or $M_{nj}(\tau)$.

The second, larger-amplitude wave arrival, depicted in Figure 9, is from a more sudden stress drop, with a rise time on the order of 500 ns. This wave arrival is of short enough duration that the P-wave and S-wave can be seen as distinct arrivals at about 4875 μs and 4892 μs, respectively, for Sensor 1. A head wave arrival can be seen on the traces from Sensors 2-4. Whereas the signals collected from the first, slower event shown in Figure 8 are difficult to interpret, the signals from the later, more rapid event contain a wealth of readily available information. For example, the location of the source of these waves was found to be of small spatial extend (less than a few mm) and located at the back end of the slider such as (e) of Figure 6. Additionally, the signals look very similar to the response to a step source, and based on the amplitude of the identifiable waves, this source is estimated to be approximately 200-400 mN in amplitude, which represents a small fraction (~3%) of the total applied shear load. Events of this type were detected on many different tests, even down to the smallest detectable amplitudes (about 10 mN in amplitude).

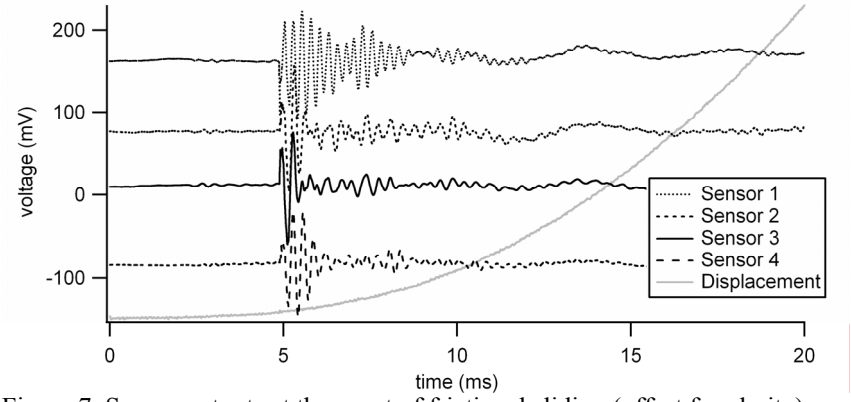

Figure 7. Sensor outputs at the onset of frictional sliding (offset for clarity).

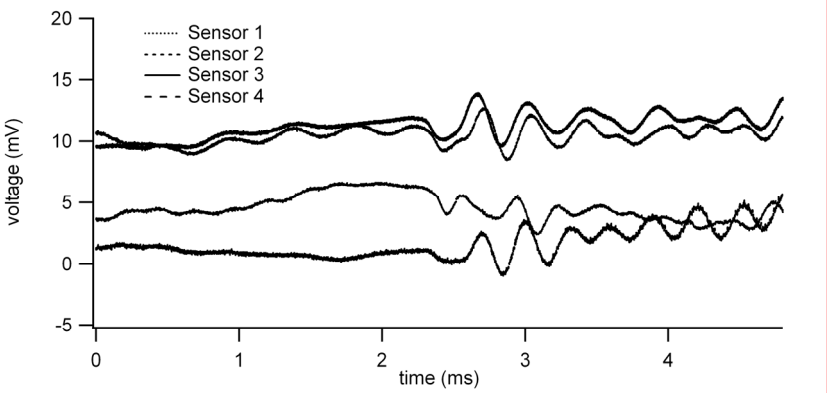

Figure 8. Sensor outputs due to a low frequency wave arrival with a rise time on the order of 100 μs.

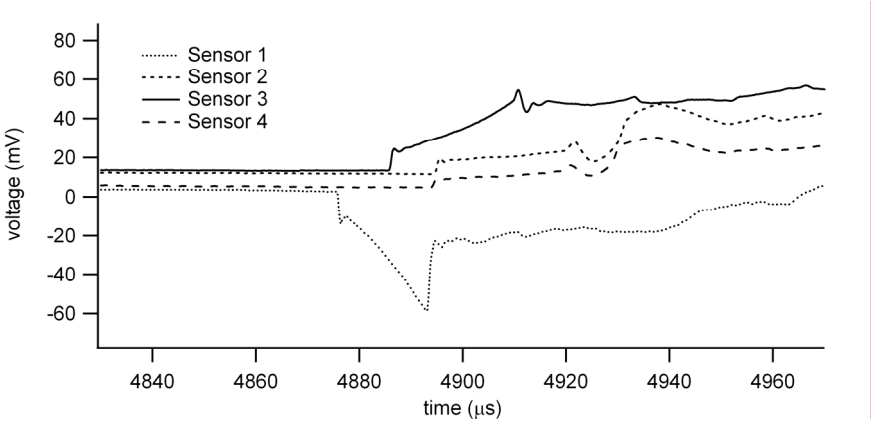

Figure 9. Sensor outputs due to a more sudden, high frequency wave arrival with a rise time on the order of 500 ns.

6 CONCLUSIONS

This work demonstrates that nanoseismic source inversion, coupled with high-fidelity sensing, can be used as a tool to study details of sliding friction, especially at the initiation of sliding. Observations were made as to phenomological similarities of frictional behaviors from the nano- to macro-scale. Solutions to the full elastodynamic equations of motion are presented in the form of a Green's function. Absolute calibration of the Glaser-NIST high-fidelity sensors used for the experiments was performed using the computed Green's functions and the known source functions from both a ball impact and a glass capillary fracture. When coupled to PMMA, the sensors have a sensitivity of 15 mV/nm ± 4 dB over a frequency range of approximately 20 kHz to 1 MHz. The calibrated noise floor for the sensors is ± 15 pm. The preliminary experiments demonstrate that local force release on the friction surface can be detected on a number of different time and amplitude scales. For rapid load releases (on the order of 500 ns) the source location can be estimated to a few mm in space and μs in time for step-like source functions down to about 10 mN in amplitude. Load releases which occur less rapidly in time (on the order of 100 μs) or over a larger spatial area (larger than a few mm) are more difficult to identify and interpret.

AKNOWLEDGEMENTS

This work was funded by NSF-GRF and NSF grant CMS-0624985.

REFERENCES

Aki, K. & Richards, P. G. 1980. *Quantitative Seismology: Theory and Methods*. Freeman: San Francisco.

Baron, J. & Ying, S. 1987. Acoustic Emission Source Location. In R. Miller, & P. McIntire (eds), *Nondestructive Testing Handbook Second Edition Vol. 5: Acoustic Emission Testing*, 136-154, American Society for Nondestructive Testing.

Bowden, F. & Tabor, D. 1950. *The Friction and Lubrication of Solids* Clarendon Press, Oxford

Breckenridge, F., Tscheigg, C., and Greenspan, M. 1975. Acoustic emission: some applications of Lamb's Problem, *J. Acoustical Soc. Am.* 57(3) 626-631.

Brune, J.N. 1973. Earthquake modeling by stick-slip along precut surfaces in stressed foam rubber. *Bulliten of the Seismological Society of America*, 63 2105 – 2119.

Burridge, R. & Knopoff, L. 1967. Model and theoretical seismicity. *Bulletin of the Seismological Society of America*, 57(3) 341-371.

Ceranoglu, A., & Pao, Y. 1981. Propagation of elastic pulses and acoustic emission in a plate. *Journal of Applied Mechanics: Transactions of the ASME* 48 125-147.

Coulomb, C.A. 1779. *Theorie des Machines Simples. Librairie Scientifique et Technique*, Albert Blanchard: Paris.
Eisenhardt, C., Jacobs, L.J. and Qu, J. 1999. Application of laser ultrasonics to develop dispersion curves for elastic plates. *Journal of Applied Mechanics.* 66(4) 1043-1045.
Glaser, S., Weiss, G., and Johnson, L. 1998. Body Waves Recorded Inside an Elastic Half-space by an Embedded, Wideband Velocity Sensor. *Journal of Acoustic Society of America*, 104, 1404-1412.
Goldsmith, W. 2001. *Impact*, Dover Publications: New York.
Graff, K. 1975. *Wave Motion in Elastic Solids.* Oxford University Press: Mineola, NY.
Greenspan, M. 1987. The NBS conical transdcuer: analysis. *J. Acoust. Soc. Of America.* 81(1) 173-183.
Hartzell, S.H. & Archuleta, R.J. 1979. Rupture propagation and focusing of energy in a foam rubber model of a stick slip earthquake. *Journal of Geophysical Research*. 84(B7) 3623-3636.
Heaton, T. 1990. Evidence for and implications of self-healing pulses of slip in earthquake rupture. *Physics of the Earth and Planetary Interiors*. 64 1-20.
Helmberger, D. 1974. Generalized ray theory for shear dislocations. *Bulletin of the Seismological Society of America*. 64(1) 45-64.
Hertz, H., 1882. U¨ber die Beru¨ hrung fester elastischer Ko¨rper. *J. Reine Angew. Mat.* 92, 156–171.
Hsu, N. & Breckenridge, F. Characterization of acoustic emission sensors. *Materials Evaluation*, 39 60-68.
Hsu, N. & Hardy, S. 1978. Experiments in Acoustic Emission Waveform Analysis for Characterization of AE Sources, Sensors and Structures. *American Society of Mechanical Engineers, Applied Mechanics Division, AMD*, 85-106.
Johnson, K. 1985. *Contact Mechanics*. Cambridge University Press: Cambridge.
Johnson, L. 1974. Green's Function for Lamb's Problem. *Geophys. J. R. astro. Soc.* 37 99-131.
Kim, K. Y. & Sachse, W. 1986. Characteristics of an acoustic emission source from a thermal crack in glass. *International Journal of Fracture.* 31 211-231.
Knopoff, L. 1958. "Surface motions of a thick plate. *J. of Applied Physics*. 29(4) 661-670.
Krim, J. Solina, D., and Chiarello, R. 1991. Nanotribology of a Kr monolayer: a quartz crystal microbalance study of atomic-scale friction. *Physical Review Letters*, 66 181-184.
Lamb, H. 1904. On the Propagation of Tremors over the Surface of an Elastic Solid. *Philosophical Transactions of the Royal Society of London A*. 203 1-42.
Love, A. 1934. *A treatise on the mathematical theory of elasticity.* Cambridge Univeristy Press: London.
McLaskey, G., Glaser, S., and Grosse, C. 2007. Integrating broad-band high-fidelity acoustic emission sensors and array processing to study drying shrinkage cracking in concrete. *Proc. of SPIE* 6529, San Diego, Mar. 18-20.
Muser, M.H. 2001. Dry friction between flat surfaces: multistable elasticity vs. material transfer and plastic deformation. *Tribology Letters*. 10(1-2) 15 – 22.
Pekeris, C. L., 1955. The Seismic Surface Pulse. *Proceedings of the National Academy of Sciences* 41 469-480.
Perrin, G., Rice, J.R., and Zheng, G. 1995. Self-healing slip pulse on a frictional surface. *Journal of the Mechanics and Physics of Solids*. 43 1461-1495.
Persson, B. 1998. *Sliding Friction*. Springer: Berlin.
Proctor, T. M. 1982. An improved piezoelectric acoustic emission transducer. *Journal of Acoustic Society of America.* 71 1163-1168.
Rayleigh, Lord, 1887. On waves propagating along the plane surface of an elastic solid. *Proc. London Mathematical Society*. 17 4-11.
Salamon, M. D. G., & Wiebols, G. A. 1974. Digital location of seismic events by an underground network of seismometers using the arrival times of compressional waves. *Rock Mechanics.* 6 141-166.
Scruby, C. & Drain, L. 1990. *Laser ultrasonics: techniques and applications*, CRC Press.
Sevinçli, H.,. Mukhopadhyay, S., Senger, R.T., and Ciraci, S. 2007. Dynamics of phononic dissipation at the atomic scale: dependence on internal degrees of freedom. *Physical Review B* 76(20) 205430.
Stein, S. & Wysession, M. 2003. *An introduction to seismology, earthquakes, and earth structure,* Blackwell: Massachusetts.
Stump, B., & Johnson, L. 1977. The determination of source properties by the linear inversion of seismograms. *Bulletin of the Seismological Society of America*. 67 1489-1502.
To, A., & Glaser, S. 2005. Full waveform inversion of a 3-D source inside an artificial rock. *Journal of Sound and Vibration*. 285 835-857.
Weiss, M. & Elmer, F-.J. 1997. Dry friction in the Frenkel–Kontorova–Tomlinson model: dynamical properties. *Zeitschrift Fur Physik B*. 104 55–69.
White, J., 1965. Seismic Waves: Radiation, Transmission, and Attenuation, McGraw-Hill: New York.